Ⓔ

Characterizing Acoustic Signals and Searching for Precursors during the Laboratory Seismic Cycle Using Unsupervised Machine Learning

by David C. Bolton, Parisa Shokouhi, Bertrand Rouet-Leduc, Claudia Hulbert, Jacques Rivière, Chris Marone, and Paul A. Johnson

ABSTRACT

Recent work shows that machine learning (ML) can predict failure time and other aspects of laboratory earthquakes using the acoustic signal emanating from the fault zone. These approaches use supervised ML to construct a mapping between features of the acoustic signal and fault properties such as the instantaneous frictional state and time to failure. We build on this work by investigating the potential for unsupervised ML to identify patterns in the acoustic signal during the laboratory seismic cycle and precursors to labquakes. We use data from friction experiments showing repetitive stick-slip failure (the lab equivalent of earthquakes) conducted at constant normal stress (2.0 MPa) and constant shearing velocity (10 μm/s). Acoustic emission signals are recorded continuously throughout the experiment at 4 MHz using broadband piezoceramic sensors. Statistical features of the acoustic signal are used with unsupervised ML clustering algorithms to identify patterns (clusters) within the data. We find consistent trends and systematic transitions in the ML clusters throughout the seismic cycle, including some evidence for precursors to labquakes. Further work is needed to connect the ML clustering patterns to physical mechanisms of failure and estimates of the time to failure.

Supplemental Content: Figures and text that describe the statistical features, sensitivity analysis of the moving windows, effects of the bandwidth parameter, and additional clustering results.

PRECURSORS TO EARTHQUAKES

Earthquake forecasting is an important problem for mitigating seismic hazard, and it can help illuminate the physics of earthquake nucleation. Forecasts could be based on physical models of the nucleation process or changes in fault-zone properties (so-called precursors) before failure. However, with current monitoring techniques and models of earthquake nucleation, we are far from forecasting earthquakes or even identifying reliable precursors despite long-standing interests in the problem (Milne, 1899; Marzocchi, 2018) and a broad range of related and direct observations ranging from landslides (Poli, 2017), to glacial motion (e.g., Faillettaz *et al.*, 2015, 2016), geochemical signals (Cui *et al.*, 2017; Martinelli and Dadomo, 2017), geodesy (Chen *et al.*, 2010; Xie *et al.*, 2016; Moro *et al.*, 2017), and seismology (Antonioli *et al.*, 2005; Niu *et al.*, 2008; Rivet *et al.*, 2011; Bouchon *et al.*, 2013). The situation is somewhat better for labquakes. Laboratory friction experiments coupled with ultrasonic measurements have been used to document the approach to failure (Scholz, 1968; Weeks *et al.*, 1978; Chen *et al.*, 1993), with important recent advances in documenting precursors based on spatiotemporal changes in rock properties before failure (Pyrak-Nolte, 2006; Mair *et al.*, 2007; Goebel *et al.*, 2013, 2015; Johnson *et al.*, 2013; Kaproth and Marone, 2013; Hedayat *et al.*, 2014; McLaskey and Lockner, 2014; Scuderi *et al.*, 2016; Jiang *et al.*, 2017; Rouet-Leduc *et al.*, 2017, 2018; Hulbert *et al.*, 2019; Renard *et al.*, 2018; Rivière *et al.*, 2018).

Laboratory observations of precursors before earthquake-like failure encompass a variety of measurements, including high-resolution images that illuminate the failure nucleation process. These include passive measurements of acoustic emissions (AEs) (e.g., McLaskey and Lockner, 2014; Goebel *et al.*, 2015), active measurements of fault-zone elastic properties (e.g., Scuderi *et al.*, 2016; Tinti *et al.*, 2016), and direct observations, using x-ray microtomography (micro-CT), of damage evolution in the failure zone (Renard *et al.*, 2017). The micro-CT work reveals microfracture patterns and the interplay between shear deformation and local volume strain (Renard *et al.*, 2017, 2018). The AE studies show that the Gutenberg–Richter *b*-value decreases systematically during the laboratory seismic cycle (Goebel *et al.*, 2013; Rivière *et al.*, 2018). In addition, active source measurements of elastic wavespeed and travel time show systematic changes throughout the laboratory seismic cycle and distinct precursors to failure for the complete spectrum of failure modes from slow to fast
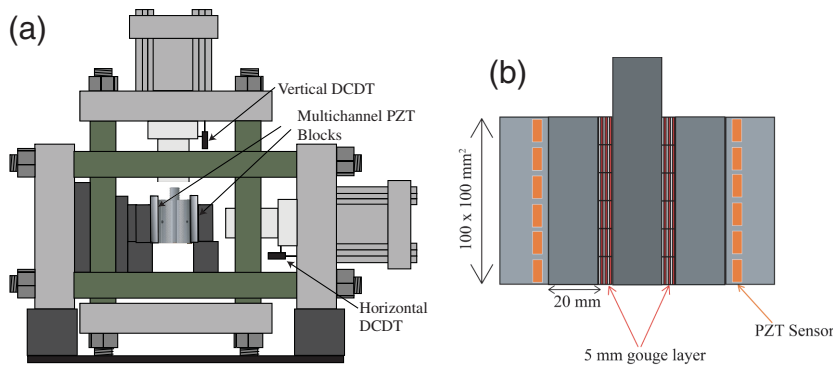
▲ **Figure 1.** (a) Biaxial shear apparatus with the double-direct shear configuration. Normal and shear forces on the fault are measured with strain-gauge load cells mounted in series with the horizontal and vertical pistons. Displacements parallel and perpendicular to the fault are measured with direct-current displacement transformers (DCDTs) coupled to the vertical and horizontal pistons, respectively. (b) Sample configuration with two gouge layers placed between three steel loading platens. Piezoceramic sensors (PZTs) are embedded within steel blocks that transmit the fault normal stress.

elastodynamic events (Kaproth and Marone, 2013; Scuderi et al., 2016; Tinti et al., 2016). These studies include measurements for dozens of repetitive stick-slip failure events showing that elastic wavespeed and transmitted amplitude increase during the linear-elastic loading stage and decrease during inelastic loading.

MACHINE LEARNING AND ACOUSTIC SIGNALS BEFORE FAILURE

Recent developments in the application of machine learning (ML) to seismic data suggest a number of possible benefits for seismic hazard analysis and earthquake prediction. One approach shows systematic changes in event occurrence patterns and seismic spectra that could illuminate the earthquake nucleation process (e.g., Holtzman et al., 2018; Wu et al., 2018). Another approach, using laboratory data similar to those that we focus on in this article, has shown that supervised ML can predict stick-slip frictional failure events—the lab equivalent of earthquakes (Rouet-Leduc et al., 2017). These works show that the timing of failure events can be predicted with fidelity using continuous records of the acoustic emissions generated within the fault zone (Rouet-Leduc et al., 2017, 2018; Hulbert et al., 2019). Stick-slip failure events are preceded by a cascade of microfailure events that radiate elastic energy in a manner that foretells catastrophic failure. Remarkably, this signal predicts the time of failure; the slip duration; and for some events, the magnitude of slip. However, successful implementation of a supervised ML algorithm demands access to a large labeled training dataset. Unsupervised ML offers an alternative approach that can be applied when labeled data are not available.

The purpose of this article is to explore the application of unsupervised ML to characterize acoustic emissions during the laboratory seismic cycle and search for precursors to failure. This approach differs significantly from previous work using supervised ML in which statistical features are used to build a function that maps an input (statistics of the acoustic signal) to an output (e.g., time to failure). Supervised ML involves a training stage followed by a stage in which the algorithm is tested against new observations. In unsupervised ML, the task at hand is quite different. In our case, the goal is to find structure (clusters) within the seismic signal and track its evolution throughout the seismic cycle. Clusters are characterized and identified within an n-dimensional feature space via an ML clustering algorithm. We use a mean-shift ML clustering algorithm (Cheng, 1995; Comaniciu and Meer, 2002) to assess statistical features of the acoustic signal and compare our results with those obtained using the commonly used k-means clustering algorithm (Tan et al., 2006). We apply both clustering algorithms to 43 statistical features after conducting a principal component analysis (PCA). For comparison to our previous work, we perform a second analysis using only the variance and kurtosis of the acoustic signal identified as the most significant features in the supervised ML analysis (Rouet-Leduc et al., 2017, 2018; Hulbert et al., 2019). That is, they improved the accuracy of the ML regression analysis the most out of ∼100 statistical features. Our goal is to assess how robust these features are when attempting to identify precursors to failure via unsupervised ML. We acknowledge that using results from a supervised ML study as inputs to an unsupervised ML analysis may violate the truly unsupervised nature of the analysis. However, we argue that this approach is well warranted because it can help connect unsupervised and supervised ML approaches. Our work has the potential to improve the understanding of laboratory precursors and ultimately to improve methods for seismic hazard analysis.

FRICTION STICK-SLIP EXPERIMENTS

We use data from frictional experiments conducted in a biaxial deformation apparatus (Fig. 1a) using the double-direct shear configuration (e.g., Rathbun and Marone, 2010). Two layers of simulated fault gouge are sheared simultaneously within three forcing blocks that contain grooves perpendicular to the shear direction to prevent shear at the layer boundary. The grooves are 0.8 mm deep and spaced every 1.0 mm. The initial gouge layer thickness is ∼5 mm, and the nominal contact area is 100×100 mm². The center forcing block (15 cm) is longer than the side blocks (10 cm) so that the friction area remains constant during shear. Our experiment used glass beads with particle diameters in the 104- to 149-μm range to simulate granular fault gouge (Anthony and Marone, 2005). The gouge layers are bounded by cellophane tape around the edges, and a thin rubber jacket is placed around the bottom half of the
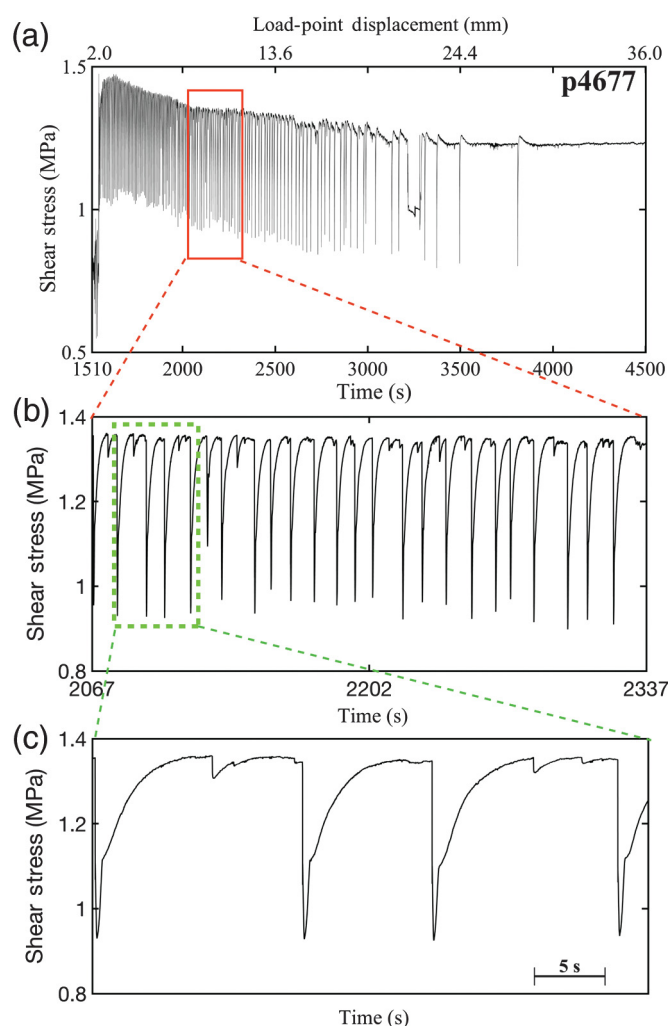
▲ **Figure 2.** (a) Shear stress evolution for one entire experiment. Slip events transition from periodic to aperiodic to stable sliding as a function of load-point displacement. We focus on (b) the section of aperiodic labquakes. Note that interevent times vary and that large events are often preceded by small foreshocks. (c) Zoom of three seismic cycles with aseismic creep and foreshocks before the main event.

sample to help prevent material loss during shear. In addition, two steel side plates are mounted over the front and back of the layers to prevent material loss from the sides (Fig. 1a).

Before shearing, the sample assembly is placed in the apparatus, and a constant normal stress boundary condition is applied perpendicular to the gouge layers. Fault normal stress is maintained constant during shear using a load-feedback servo control. After the sample has compacted, the central forcing block is driven down at a constant velocity to impose fault-zone shear (Fig. 1a). Displacements parallel and perpendicular to the fault are measured using direct-current displacement transformers, which are coupled directly to the vertical and horizontal pistons. Similarly, forces parallel and perpendicular to the fault are measured with load cells and are mounted in series with vertical and horizontal pistons. Stresses and displacements are recorded

continuously throughout the experiment at 1 kHz with a 24-bit, ±10-V data acquisition system.

We measure elastic waves generated within the fault zones using an array of 36 P-polarized piezoceramic transducers (Fig. 1). The sensors (6.35 mm in diameter and 4 mm thick) are epoxied in the bottom of blind holes within steel blocks that flank the side forcing blocks (Fig. 1b). The blind holes (18 mm deep and 8 mm in diameter) are filled with epoxy to hold the sensors and their respective cables in place (Rivière *et al.*, 2018). The sensor array is located ∼22 mm from the edge of the gouge layers (Fig. 1b). Acoustic emission data are sampled continuously at 4 MHz using a 14-bit Verasonics data acquisition system (Rivière *et al.*, 2018). Here, we show results from one of the 36 channels, which was chosen as representative based on calibrations and analysis of all channels.

Our database for these experiments includes more than 50 experiments. We focus here on a few select runs, conducted at constant normal stress of 2.0 MPa and a constant shearing velocity of 10 μm/s. These experiments include many stick-slip cycles. After ∼10 mm of shear (see upper x-axis label in Fig. 2a), slip events include periodic and aperiodic behavior (Fig. 2a,b). We analyze a section of ∼25 stick-slip cycles of the experiment where the recurrence interval between failure events is aperiodic (Fig. 2). These data are representative of our complete dataset. Each stick-slip cycle is characterized by a linear-elastic loading stage followed by inelastic loading. The departure from linear-elastic loading denotes the onset of fault creep (Anthony and Marone, 2005; Johnson *et al.*, 2008). We observe a range of failure events including creep, small stick-slip events, and larger events that define the overall lab seismic cycle (Fig. 2c). Acoustic data for a representative lab seismic cycle are shown along with a zoom during the linear-elastic loading stage (Fig. 3). On average, we detect several thousand AEs, including small (Fig. 3c) and large AEs (Fig. 3d), as defined by their amplitudes and durations. We observe a nonlinear increase in the amplitude and number of acoustic events as the fault approaches failure (Fig. 3), with AE amplitude increasing by three orders of magnitude (e.g., Rivière *et al.*, 2018).

UNSUPERVISED ML ANALYSIS OF ACOUSTIC SIGNALS

We implement two clustering algorithms to find systematic trends in the continuous acoustic signal emanating from the fault zone throughout the laboratory seismic cycle. Clustering is an unsupervised ML analysis used to identify structures within a dataset and partition the data into distinct groups called clusters based on prescribed similarity measures (Jain *et al.*, 1999). We focus on statistics of the continuous acoustic signal (features) and use a cluster analysis to find groups of similar data (clusters). The clusters and their member data points are, in general, functions of all n statistical features that define the feature space as well as the similarity measure.

Our dataset consists of statistical features that quantify both the amplitude and frequency content of the acoustic emission time series. Following Rouet-Leduc *et al.* (2017), we
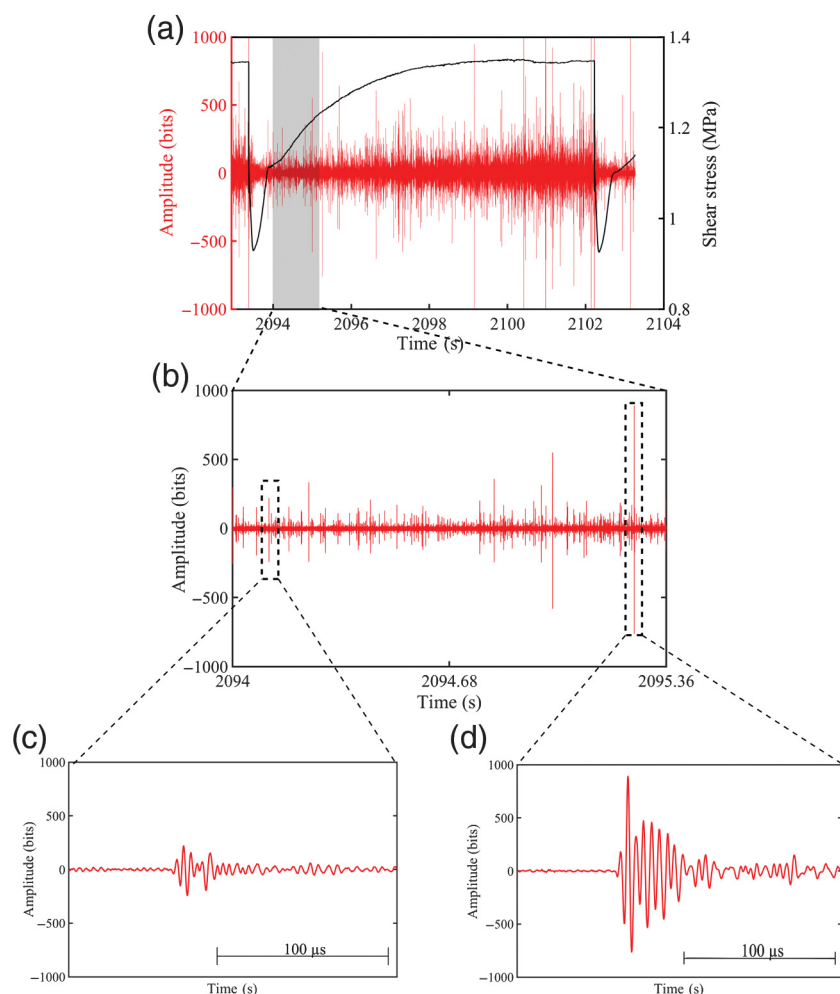
▲ **Figure 3.** (a) Shear stress and acoustic amplitude plotted for one slip cycle within the aperiodic section of the experiment (see Fig. 2). Gray box shows a 1.36-s moving window used to compute statistical features of the acoustic signal. (b) Zoom of the window. Note that the signal is dominated by spikes that look like noise at this scale. (c) Small AEs occur frequently throughout all stages of the seismic cycle. (d) Large AEs occur during all stages of the laboratory seismic cycle; however, they are more commonly associated with the inelastic loading stage just before failure (see Fig. 2).

compute a total of 43 statistical features of the acoustic signal using a moving-window approach (see the Ⓔ Supplemental Content, available in this article for details). Our acoustic data are recorded at 4 MHz, and we calculate statistics in a time window 1.36 s in length. Windows overlap by 90%, and we use a backward-looking approach to time stamp the data for comparison with our mechanical data (e.g., stress and displacement) recorded at 1 kHz. The ML analysis is conducted using data between 2067 and 2337 s; this results in a 1979 by 43 data matrix. Details of the statistical features along with a sensitivity analysis of window size and overlap are given in the Ⓔ Supplemental Content.

A range of clustering algorithms are available, many of which make predefined assumptions about the data that can induce bias (Tan *et al.*, 2006). Specifically, many algorithms

require the number of clusters to be known *a priori* and assume each cluster is characterized by a specific shape (e.g., an ellipse). To avoid making these assumptions, we implemented the mean-shift clustering algorithm from scikit-learn, which seeks to identify the modes of the dataset (Comaniciu and Meer, 2002). In addition to mean shift, we use the scikit-learn implementation of a *k*-means clustering algorithm for comparison.

In mean shift, modes are found through an iterative process of computing a mean-shift vector over a spatial region defined by a bandwidth parameter within an *n*-dimensional feature space. Because the bandwidth has to be known *a priori*, we optimize the bandwidth by selecting the value that yields the highest silhouette coefficient (Rousseeuw, 1987; Tan *et al.*, 2006; see the Ⓔ Supplemental Content). In the following, we give a brief summary of how this algorithm works in a 2D feature space. For a more thorough mathematical explanation of the algorithm, we refer readers to Cheng (1995) and Comaniciu and Meer (2002). The algorithm commences by computing the mean of data points within a window of feature space. In this context, "window" refers to a bounded region in the feature space. The size of this bounded region is set beforehand via the bandwidth parameter (Cheng, 1995; Comaniciu and Meer, 2002). The bandwidth sets the size over which the mean is computed within *n*-space and thus controls the total number of clusters as well as the number of data points mapped to each cluster (see the Ⓔ Supplemental Content). The mean of the data points within this confined window corresponds to the densest region in the window. A vector is then defined from the center of the window to the calculated mean, which is called the mean-shift vector. In the next iteration, the window is shifted such that the mean of the previous distribution of data points is now the center of the current window. As a result of this shift, whereas some data points move out of the window, others move in. Again, the mean of the data points is computed within the window, and the mean-shift vector is calculated. This iterative process continues until the mean-shift vector approaches zero, that is, the center of the window coincides with the densest region in the feature space. The process of computing the mean-shift vector over a predefined space is repeated for every data point within the feature space (i.e., it is initialized for every data point). After this process is completed, each data point will be assigned to a specific region (a mode) in the feature space that it converged to. One way of thinking about this process is that all data points have a trajectory in feature space that they follow, and their final location
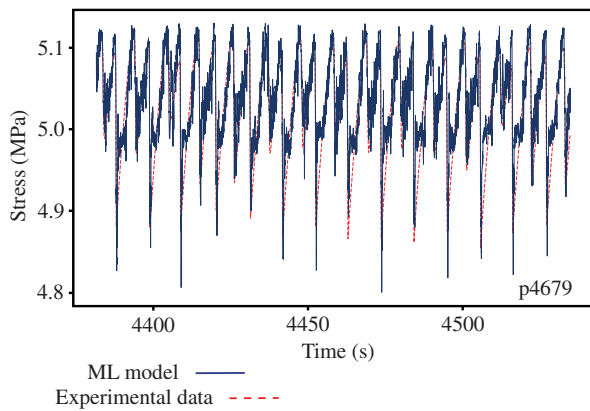
▲ **Figure 4**. Shear stress as a function of time (red dashed line) plotted with the machine learning (ML) prediction (blue line) for experiment p4679. Here, a supervised ML algorithm (gradient boosted tree algorithm) is used to estimate the instantaneous shear stress based on similar statistical features used in this study (see the Ⓔ Supplemental Content, available in this article). The tight correlation between measurements and the ML prediction shows that the acoustic signal contains important information regarding the physical state of the fault during all stages of the lab seismic cycle (after Hulbert *et al.,* 2019).

represents the densest region in feature space based on that path. In other words, the total number of modes found after this step will equal the number of data points. As a final step, the algorithm filters out modes that lie within a bandwidth of one another. Specifically, the modes, which have the least number of data points within them, are removed. The result of this process is a unique set of modes that model the underlying feature space.

Our analysis consists of clustering all 43 features after performing a PCA. In addition, we perform a second analysis where we focus on variance and kurtosis, the two most important features for predicting instantaneous friction and time to failure of labquakes through supervised ML (Rouet-Leduc *et al.,* 2017). In fact, the variance alone can accurately predict the instantaneous frictional state along with the magnitude of slip events (Rouet-Leduc *et al.,* 2018; Hulbert *et al.,* 2019) as illustrated in Figure 4. In our analysis, we use the logarithms of the variance and kurtosis as a way to normalize their values, given that kurtosis ranges up to $> 10^4$, but variance is typically an order of magnitude smaller. If clustering is performed without normalization, the results would be biased toward kurtosis (see the Ⓔ Supplemental Content). The purpose of this second study is to compare the supervised and unsupervised ML approaches. It is established that a supervised ML technique can predict labquakes and hence that the acoustic signal contains information about impending failure during all times of the seismic cycle. In this work, we seek to determine if unsupervised ML can identify patterns and precursors to failure. To our knowledge, using unsupervised ML to identify precursors to stick-slip failure is a new approach that has yet to be explored. Moreover, an unsupervised ML approach could be

more applicable to field data, in which labeled data (e.g., shear stress, time to failure) are typically unavailable.

CLUSTERING IN PRINCIPAL COMPONENT SPACE

To test the full set of 43 statistical features, we perform a PCA. PCA offers several incentives for our analysis. First, it identifies the most important features for explaining the data variance. Second, it enables us to reduce the dimensionality of our problem while still exploiting all 43 features. Finally, it identifies correlated features. After performing the PCA, we can project our dataset into a lower dimension principal component (PC) space and perform the clustering analysis in this space. Specifically, PCA is an eigenvalue decomposition of the covariance matrix. Before calculating the covariance matrix, the original 1479 by 43 data matrix is normalized by subtracting the mean and dividing by the standard deviation. The decomposition of this covariance matrix gives a set of eigenvalues and eigenvectors (PCs), both of which can be used to describe the structure of the data. In particular, each PC is a linear combination of the original features, scaled by an eigenvector coefficient (see the Ⓔ Supplemental Content). In addition, the PCs are ordered such that by selecting the first few PCs, we can capture most of the data variance (see Fig. 5c) while reducing the dimensionality of the problem.

Our PCA results show that the first two PCs account for about 85% of the total data variance (Fig. 5c). This implies that we can represent our original 43D space in a 2D PC space (Fig. 5). When projected into the 2D PC space, the acoustic data appear in groups of different shape and density. For example, a subset of data points form distinct streaks that extend from the top left to the bottom right of this space. A careful examination of the temporal trends of PC 1 and PC 2 shown in Figure 5b reveal that these data points correspond to the interseismic period. The remaining data points in Figure 5d represent data from the coseismic slip phase. These data have a different structure than the interseismic period and plot in a different region within the feature space (i.e., on the left side of Fig. 5d). All data from Figure 2b are plotted in Figure 5d, and thus, it is clear that these trends are remarkably systematic across multiple labquake cycles. We use clustering to identify such patterns in the acoustic data statistics and study them in relation to the seismic cycle.

RESULTS

In Figure 6, we demonstrate how mean shift and *k*-means partition both feature spaces explored in this study. The mean-shift algorithm identifies two clusters (defined by the red and cyan symbols) with respect to variance and kurtosis (Fig. 6a). The red cluster is defined by areas of low variance and kurtosis values, and the cyan cluster defines areas of high variance and kurtosis. When using *k*-means, the number of clusters the algorithm finds must be set *a priori* (Tan *et al.,* 2006). Therefore, we use the silhouette coefficient to find the optimal number of clusters. That is, we select the number of clusters that results in the highest silhouette coefficient. In variance–kurtosis space
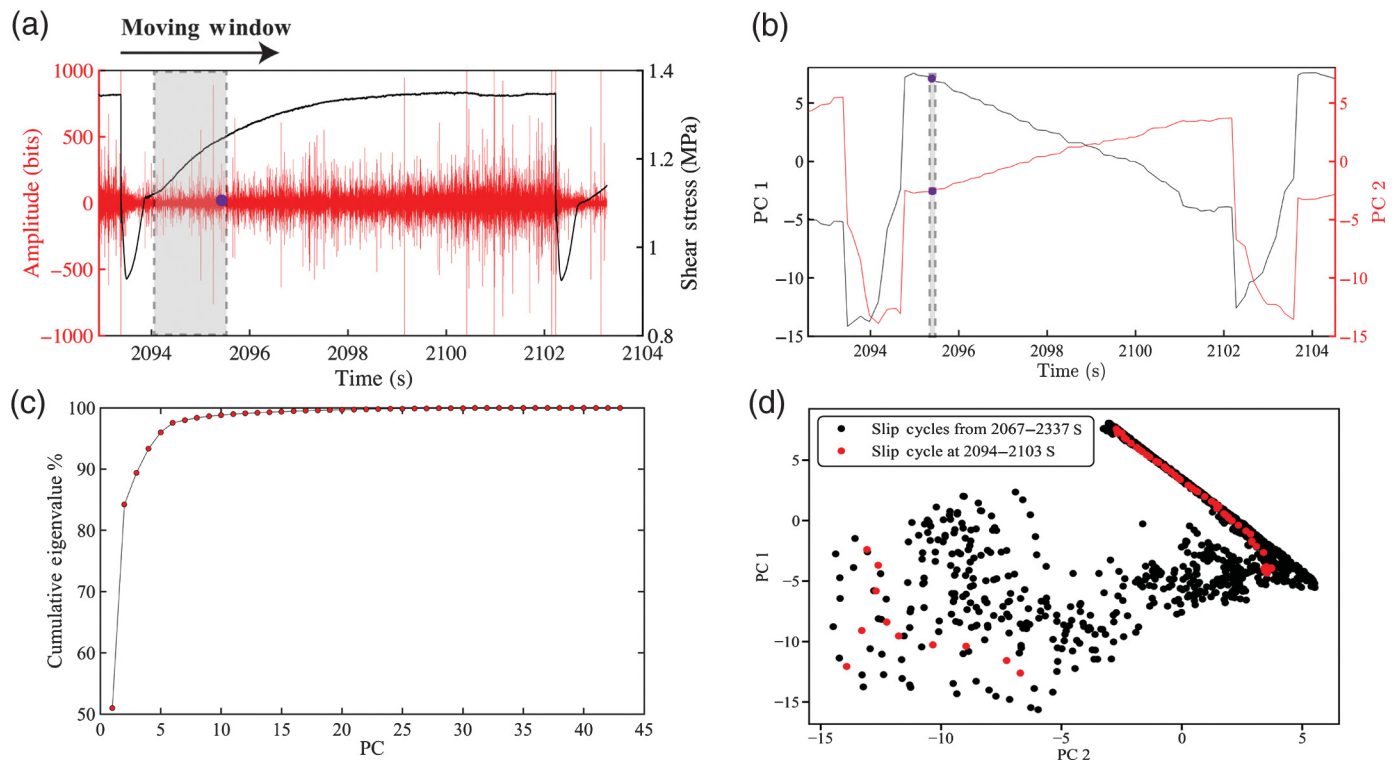
▲ **Figure 5.** (a) Shear stress evolution and acoustic amplitude for one stick-slip cycle in experiment p4677. Gray box shows a moving window that slides through the continuous time series (4 MHz sampling rate) and is used to compute statistical features of the acoustic signal. We use the end time of each window for the time stamp associated with the window. (b) Temporal evolution of principal component (PC) 1 (black) and PC 2 (red) throughout one stick-slip cycle shown in (a). Gray box with circles shows the time stamp derived from the moving window in (a). (c) Cumulative eigenvalue percentage plotted versus number of PCs. The first two PCs account for about 85% of the data variance. (d) Data for all slip cycles between 2067 and 2337 s (Fig. 2b) in PC 1–PC 2 space (black symbols). Highlighted in red are data for the slip cycle shown in (a).

(Fig. 6c), k-means also partitions the data into two clusters. More interestingly, the two sets of clusters found by the two algorithms in variance–kurtosis space are identical (Fig. 6c). Figure 6b,d shows how both algorithms partition the data in PC space. The mean shift identifies a total of four clusters (denoted by yellow–magenta–green–blue symbols). Although the boundaries between clusters may seem arbitrary in this space, when plotted as a function of time or shear stress, it becomes clear that these boundaries mark specific transitions with respect to the stress state (Figs. 7 and 8). We cluster the same data using the k-means algorithm with the number of clusters set to three. Again, we determine the number of clusters based on the maximum silhouette coefficient. Despite the differences in the number of identified clusters, the results from the two algorithms are effectively the same; the only differences lie in how the algorithms partition the data associated with the coseismic slip phase (i.e., green–blue data points). For mean shift, the coseismic data are partitioned into two clusters (blue–green), but with k-means, these data are partitioned into only one cluster (green). Because we are primarily interested in identifying precursors to failure, the data associated with the coseismic phase are of less importance. Furthermore, we conducted the same analysis using a spectral clustering algorithm and achieved

similar results. Therefore, we argue that our analysis does not depend on the choice of the clustering algorithms. From here forward, we present all results with respect to mean shift.

As previously stated, the mean-shift analysis identifies four clusters in PC space (Fig. 6b). To observe how clusters evolve temporally over the course of the lab seismic cycle, we plot data from Figure 6b as a function of time together with shear stress (Fig. 7). Whereas the yellow and magenta clusters coincide with the linear-elastic loading and creep stages, the green and blue clusters coincide with the main slip events (Fig. 7). Clustering in PC space also reveals precursory changes in the acoustic signal as the fault approaches failure, and as result, we observe that the interseismic period of each slip cycle is characterized by two clusters (Figs. 7 and 8). When performing the same analysis with respect to variance and kurtosis, we did not observe such systematic change in clusters (Ⓔ Fig. S10). Specifically, when clustering data in variance–kurtosis space, we observe two clusters before the main slip event only when there are small instabilities during aseismic creep. In contrast, the systematic transitions of clusters in PC space are observed for every slip cycle analyzed. In addition, both PC 1 and PC 2 show similar precursory trends (see the Ⓔ Supplemental Content for PC 2 results plotted with time).
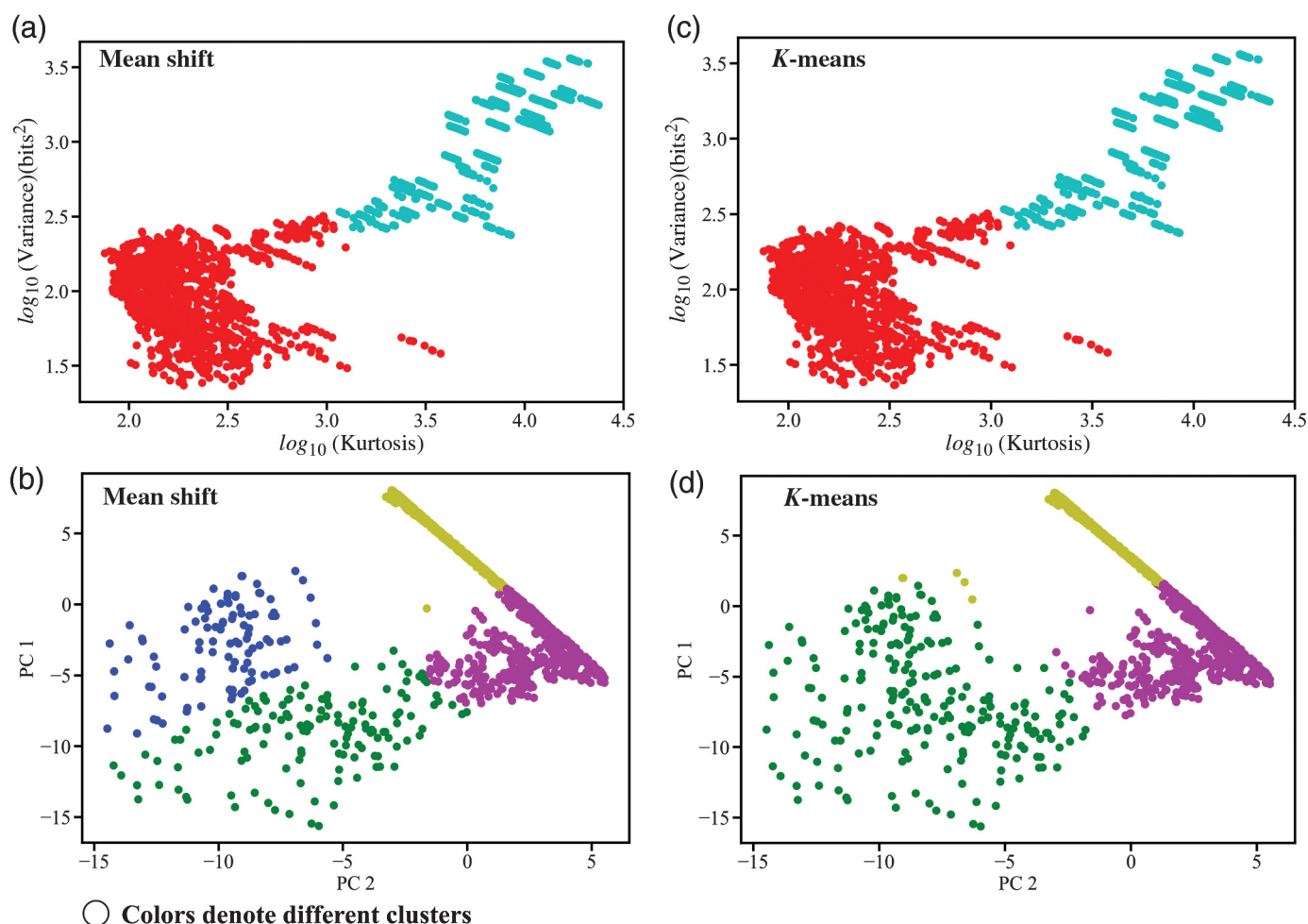
▲ **Figure 6.** (a,b) Data for all stick-slip cycles analyzed in this study (see Fig. 2b) after clustering with a mean-shift algorithm. (a) Results for acoustic variance and kurtosis. Whereas the red cluster encompasses all data that are not associated with a labquake, the cyan cluster classifies the acoustic data associated with both foreshocks and mainshocks (see Fig. 2c). (b) Results for PC 1 and PC 2 after clustering in PC space. Each point represents a linear combination of the 43 statistical features, and each color corresponds to a single cluster. Whereas the yellow and magenta clusters classify the acoustic signal associated with the linear-elastic and inelastic loading stages of each seismic cycle, the green and blue clusters classify the acoustic data associated with the coseismic phase. (c,d) Results after clustering with a *k*-means algorithm. In each case, we determine the number of clusters by optimizing the silhouette coefficient as a function of the number of clusters (see the Ⓔ Supplemental Content). Note that the results are identical for *k*-means and mean shift when clustering in variance–kurtosis space. When clustering in PC space, the acoustic data associated with the interseismic period (i.e., yellow and magenta clusters) are independent of the choice of clustering algorithm. However, the coseismic data are partitioned differently by the two clustering algorithms (i.e., green and blue clusters).

Figures 7 and 8 suggest that the partitioning of the acoustic data into four clusters is purely a function of position within the stick-slip cycle. Specifically, whereas the yellow and magenta cluster corresponds to the linear and nonlinear loading stages of the stick-slip cycle, the green and blue clusters mark the slip event (Fig. 7). The transition from yellow to magenta clusters occurs when the fault has reached peak strength and the shear stress is no longer increasing. This is an interesting discovery given that the clustering algorithm has no input on the stress state of the fault, yet the results clearly show when the fault has reached its peak strength (Fig. 8). Finally, the division between the green and blue clusters occurs during the coseismic stage as

the fault evolves from a large (green cluster) to a small (blue cluster) shear stress.

DISCUSSION

We show that an unsupervised ML approach based on a clustering analysis of acoustic data define distinct clusters that evolve systematically during the lab seismic cycle. Clustering in PC space partitions the dataset into four clusters, including two distinct clusters for the interseismic period (Figs. 7a,b and 8). The temporal evolution of these clusters shows that within each seismic cycle, there is a cluster transition when the fault begins to
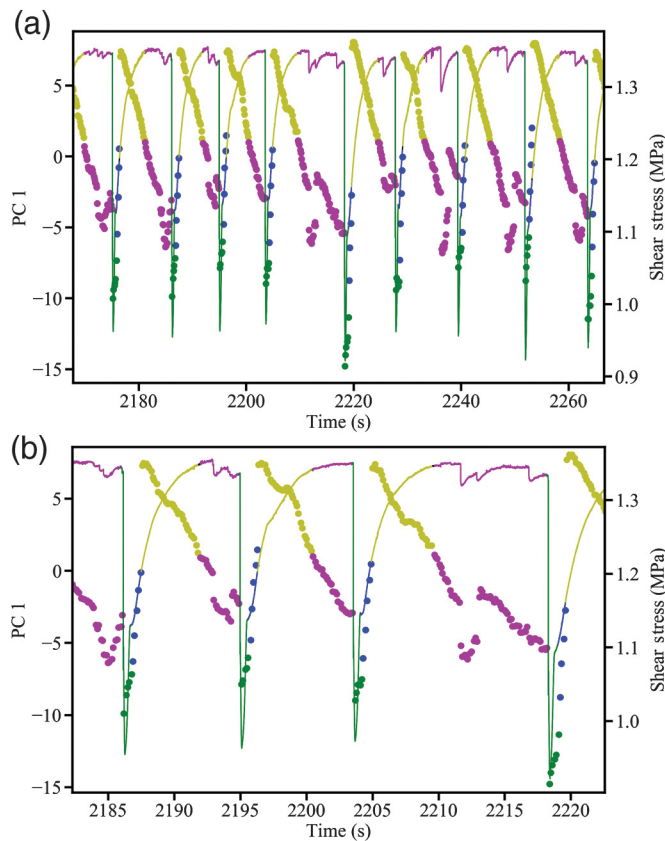
▲ **Figure 7.** (a) Temporal evolution of clusters with respect to PC 1 (see the Ⓔ Supplemental Content for results for PC 2). Shear stress curves are color coded corresponding to their respective cluster color defined by PC 1 and PC 2. The clusters reveal a distinct and systematic temporal trend as failure approaches. (b) Zoom showing details of how the clusters evolve as failure approaches. Whereas the early stages of the interseismic period are mapped to the yellow cluster, the latter stages are mapped to the magenta cluster. The coseismic phase is further divided into the green and blue clusters.

creep at a shear stress near its maximum value followed by separate transitions during the main failure event (Figs. 7 and 8). The cluster transitions for PC 1 and PC 2 provide information about what stage the fault is in within its seismic cycle, and thus, could be identified as potential precursors to failure. Specifically, the yellow cluster is associated with shear loading, and thus, indicates that the fault is in its earliest stage of the seismic cycle (Fig. 8). However, the magenta cluster is associated with the latter stages of the seismic cycle and denotes that the fault is creeping and is close to failure (Fig. 8).

In a previous study, we found that out of ∼100 statistical features, the variance and kurtosis are the most important features when building the ML regression model. However, this study demonstrates that the clustering of data based on these two features is unable to identify precursors (Ⓔ Fig. S10). Even though the resulting clusters define a systematic pattern during the seismic cycle, the transition between clusters occurs after failure and thus provides no precursory information to failure
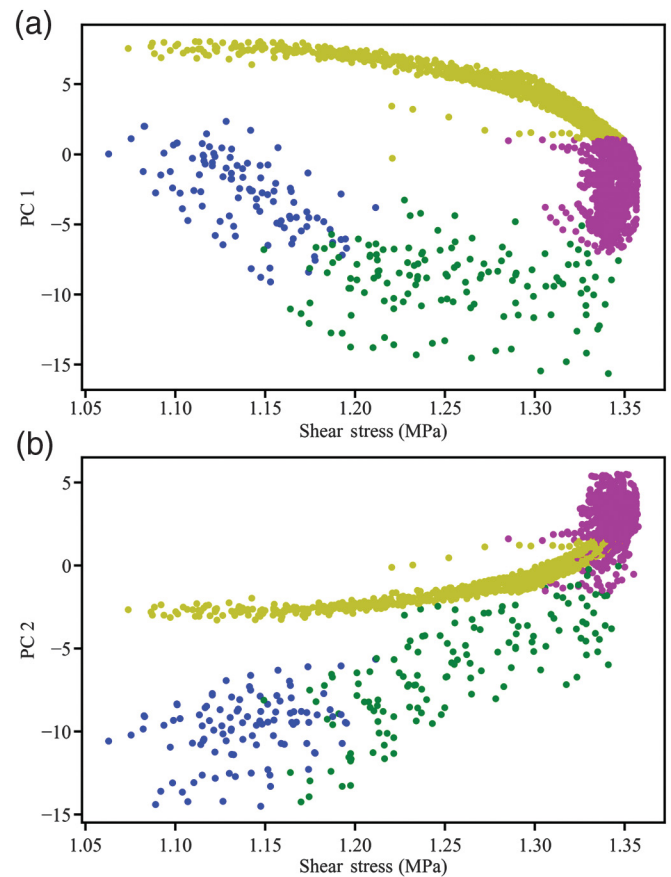
▲ **Figure 8.** Comparison of PC 1 and PC 2 as a function of shear stress. In (a,b), we plot data for all seismic cycles analyzed in this study (Fig. 2b), color coded by cluster. Note that the partitioning of data into clusters by the ML algorithm is reproducible across multiple lab seismic cycles and labquakes. Plotting the acoustic data as a function of shear stress illuminates the relationship between cluster transitions (e.g., yellow to magenta), and it becomes clear that the transition from yellow to magenta occurs when the fault has reached its peak strength. Acoustic data associated with the coseismic phase are mapped to the green and blue clusters.

(Ⓔ Fig. S10). The majority of the laboratory seismic cycle is mapped into one cluster, but small segments associated with slip events are assigned to another cluster. This implies that even though signal variance and kurtosis are evolving throughout the course of a stick-slip cycle, these parameters do not change enough to result in separate clusters.

We show that the differences between clustering in PC space and clustering in variance–kurtosis space are from the features themselves and not the number of clusters (see the Ⓔ Supplemental Content for details). The data suggest that although it is possible to identify four clusters when clustering in variance–kurtosis space, the clusters themselves are not systematic across multiple slip cycles. In particular, one of the clusters is associated with only five slip cycles. Moreover, none of the four identified clusters in the variance–kurtosis space are correlated to fault strength. Therefore, we hypothesize that the

differences found in the PCA result from differences in the features themselves and not the number of clusters found.

One potential drawback of clustering in PC space is the loss of a physical meaning behind the clusters; because each PC is a linear combination of 43 features scaled by an eigenvector coefficient. Our data show that the coefficients for the first two PCs are similar for most features, implying that they are equally important in explaining the data variance (see the Ⓔ Supplemental Content). However, several of the amplitude-based features in PC 1 and PC 2 have large coefficients relative to other features, indicating that they are more important relative to the other features in explaining the data variance.

Our ML approach compares well with the traditional approach of monitoring failure in the laboratory using the *b*-value of AE events (Goebel *et al.*, 2013; Rivière *et al.*, 2018). However, our approach extends to both quasiperiodic failure events and aperiodic failure events with significant fault creep and minor events associated with small stress drops (Fig. 8). A key problem with application of *b*-value to failure prediction is that it often shows a continuous decrease as failure approaches (Goebel *et al.*, 2013; Rivière *et al.*, 2018), without any clear connection to the time to failure. The clustering in variance–kurtosis space shows a similar limitation, but results in PC space suggest that with additional features, the cluster transitions could be related quantitatively to the time to failure.

A comparison of the methods explored in this study suggests that clustering in PC space offers a more systematic and reliable precursor trends to failure. The clusters defined by the PCs show systematic changes as failure approaches. These changes occur for every slip cycle analyzed, and they occur at the same points during the lab seismic cycle (Fig. 8). However, further work is needed to provide better temporal resolution and to document precursory trends for a wider range of conditions. One possibility is that additional information could be found using another ML algorithm, different statistical features, or with a more direct connection between an unsupervised ML approach and supervised ML. These are useful directions for further study.

CONCLUSIONS

We explore the use of unsupervised ML for characterizing acoustic signals during the laboratory seismic cycle. We apply an unsupervised ML technique to a known dataset, for which supervised ML can predict the time to failure for repetitive failure events. Overall, the unsupervised approach is less informative of the physical state of the fault than its supervised counterpart. However, the unsupervised ML cluster analysis is successful in identifying patterns in the statistics of acoustic signals throughout the seismic cycle when using all 43 statistical features. Clusters formed from the two most important features identified by supervised ML analysis, variance and kurtosis, define transitions but these do not provide reliable new information on impending failure. However, the ML cluster analysis using the two primary eigenvectors defined by a PCA of all 43 statistical features of the continuous acoustic signal reveals clear precursors to failure. The

precursors are identified in all slip cycles analyzed and occur when the fault has reached its peak strength.

Both of our cluster analyses are consistent with temporal trends observed in the seismic *b*-value over the complete cycle of shear loading to failure (Rivière *et al.*, 2018). We find that although it is possible to infer the stress state of a laboratory fault during the laboratory seismic cycle with supervised ML, such detailed information cannot be found when feeding the same statistics into an unsupervised ML algorithm. Nonetheless, the simplicity of unsupervised ML compared with supervised approaches and the fact that it does not require large labeled training datasets is likely to make it a valuable complementary tool when tackling large-scale data. Our work shows that unsupervised ML algorithms hold promise for identifying precursors to seismic failure; however, further work is necessary to develop this approach into a reliable tool that could have an impact in seismic hazard analysis.

DATA AND RESOURCES

All data used in this article were collected at The Pennsylvania State University Rock and Sediment Mechanics Laboratory. ⬔

REFERENCES

Anthony, J. L., and C. Marone (2005). Influence of particle characteristics on granular friction, *J. Geophys. Res.* **110,** no. B8, doi: 10.1029/2004JB003399.

Antonioli, A., D. Piccinini, L. Chiaraluce, and M. Cocco (2005). Fluid flow and seismicity pattern: Evidence from the 1997 Umbria-Marche (central Italy) seismic sequence, *Geophys. Res. Lett.* **32,** L10311, doi: 10.1029/2004GL022256.

Bouchon, M., V. Durand, D. Marsan, H. Karabulut, and J. Schmittbuhl (2013). The long precursory phase of most large interplate earthquakes, *Nature Geosci.* **6,** no. 4, 299.

Chen, J. H., B. Froment, Q. Y. Liu, and M. Campillo (2010). Distribution of seismic wave speed changes associated with the 12 May 2008 M_w 7.9 Wenchuan earthquake: Wave speed changed by the Wenchuan earthquake, *Geophys. Res. Lett.* **37,** L18302, doi: 10.1029/2010GL044582.

Chen, W. Y., C. W. Lovell, G. M. Haley, and L. J. Pyrak-Nolte (1993). Variation of shear-wave amplitude during frictional sliding, *Intl. J. Rock Mech. Min. Sci. Geomech. Abstr.* **30,** no. 7, 779–784.

Cheng, Y. (1995). Mean shift, mode seeking, and clustering, *IEEE Trans. Pattern Anal. Mach. Intell.* **17,** no. 8, 790–799.

Comaniciu, D., and P. Meer (2002). Mean shift: A robust approach toward feature space analysis, *IEEE Trans. Pattern Anal. Mach. Intell.* **24,** no. 5, 603–619.

Cui, Y., D. Ouzounov, N. Hatzopoulos, K. Sun, Z. Zou, and J. Du (2017). Satellite observation of CH4 and CO anomalies associated with the Wenchuan M_S 8.0 and Lushan M_S 7.0 earthquakes in China, *Chem. Geol.* **469,** 185–191, doi: 10.1016/j.chemgeo.2017.06.028.

Faillettaz, J., M. Funk, and C. Vincent (2015). Avalanching glacier instabilities: Review on processes and early warning perspectives, *Rev. Geophys.* **53,** no. 2, 203–224.

Faillettaz, J., D. Or, and I. Reiweger (2016). Codetection of acoustic emissions during failure of heterogeneous media: New perspectives for natural hazard early warning, *Geophys. Res. Lett.* **43,** no. 3, 1075–1083.

Goebel, T. H. W., C. G. Sammis, T. W. Becker, G. Dresen, and D. Schorlemmer (2015). A comparison of seismicity characteristics and fault structure between stick-slip experiments and nature, *Pure Appl. Geophys.* **172,** no. 8, 2247–2264.

Goebel, T. H. W., D. Schorlemmer, T. W. Becker, G. Dresen, and C. G. Sammis (2013). Acoustic emissions document stress changes over many seismic cycles in stick-slip experiments, *Geophys. Res. Lett.* **40,** no. 10, 2049–2054, doi: 10.1002/grl.50507.

Hedayat, A., L. J. Pyrak-Nolte, and A. Bobet (2014). Precursors to the shear failure of rock discontinuities, *Geophys. Res. Lett.* **41,** no. 15, 5467–5475.

Holtzman, B. K., A. Paté, J. Paisley, F. Waldhauser, and D. Repetto (2018). Machine learning reveals cyclic changes in seismic source spectra in Geysers geothermal field, *Sci. Adv.* **4,** no. 5, eaao2929.

Hulbert, C., B. Rouet-Leduc, P. A. Johnson, C. X. Ren, J. Rivière, D. C. Bolton, and C. Marone (2019). Similarity of fast and slow earthquakes illuminated by machine learning, *Nature Geosci.* **12,** no. 1, 69.

Jain, A. K., M. N. Murty, and P. J. Flynn (1999). Data clustering: A review, *ACM Comput. Surv.* **31,** no. 3, 264–323.

Jiang, Y., G. Wang, and T. Kamai (2017). Acoustic emission signature of mechanical failure: Insights from ring-shear friction experiments on granular materials, *Geophys. Res. Lett.* **44,** no. 6, 2782–2791.

Johnson, P. A., B. Ferdowsi, B. M. Kaproth, M. M. Scuderi, M. Griffa, J. Carmeliet, R. A. Guyer, P.-Y. Le Bas, D. T. Trugman, and C. Marone (2013). Acoustic emission and microslip precursors to stick-slip failure in sheared granular material, *Geophys. Res. Lett.* **40,** no. 21, 5627–5631, doi: 10.1002/2013GL057848.

Johnson, P. A., H. Savage, M. Knuth, J. Gomberg, and C. Marone (2008). Effects of acoustic waves on stick-slip in granular media and implications for earthquakes, *Nature* **451,** no. 7174, 57.

Kaproth, B. M., and C. Marone (2013). Slow earthquakes, preseismic velocity changes, and the origin of slow frictional stick-slip. *Science* **341,** no. 6151, 1229–1232.

Mair, K., C. Marone, and R. P. Young (2007). Rate dependence of acoustic emissions generated during shear of simulated fault gouge, *Bull. Seismol. Soc. Am.* **97,** no. 6, 1841–1849, doi: 10.1785/0120060242.

Martinelli, G., and A. Dadomo (2017). Factors constraining the geographic distribution of earthquake geochemical and fluid-related precursors, *Chem. Geol.* **469,** 176–184.

Marzocchi, W. (2018). Predictive seismology, *Seismol. Res. Lett* **89,** no. 6, doi: 10.1785/0220180238.

McLaskey, G. C., and D. A. Lockner (2014). Preslip and cascade processes initiating laboratory stick slip, *J. Geophys. Res.* **119,** no. 8, 6323–6336.

Milne, J. (1899). Earthquake precursors, *Nature* **59,** no. 1531, 414.

Moro, M., M. Saroli, S. Stramondo, C. Bignami, M. Albano, E. Falcucci, S. Gori, C. Doglioni, M. Polcari, M. Tallini, *et al.* (2017). New insights into earthquake precursors from InSAR, *Sci. Rept.* **7,** no. 1, 12,035.

Niu, F., P. G. Silver, T. M. Daley, X. Cheng, and E. L. Majer (2008). Preseismic velocity changes observed from active source monitoring at the Parkfield SAFOD drill site, *Nature* **454,** no. 7201, 204.

Poli, P. (2017). Creep and slip: Seismic precursors to the Nuugaatsiaq landslide (Greenland), *Geophys. Res. Lett.* **44,** no. 17, 8832–8836.

Pyrak-Nolte, L. (2006). Monitoring a propagating front: Exploiting Fresnel precursors from fractures, *Golden Rocks 2006, The 41st US Symposium on Rock Mechanics (USRMS)*, Golden, Colorado, 17–21 June, American Rock Mechanics Association.

Rathbun, A. P., and C. Marone (2010). Effect of strain localization on frictional behavior of sheared granular materials, *J. Geophys. Res.* **115,** no. B1, doi: 10.1029/2009JB006466.

Renard, F., B. Cordonnier, M. Kobchenko, N. Kandula, J. Weiss, and W. Zhu (2017). Microscale characterization of rupture nucleation unravels precursors to faulting in rocks, *Earth Planet. Sci. Lett.* **476,** 69–78.

Renard, F., J. Weiss, J. Mathiesen, Y. Ben-Zion, N. Kandula, and B. Cordonnier (2018). Critical evolution of damage toward system-size failure in crystalline rock, *J. Geophys. Res.* **123,** no. 2, 1969–1986.

Rivet, D., M. Campillo, N. M. Shapiro, V. Cruz-Atienza, M. Radiguet, N. Cotte, and V. Kostoglodov (2011). Seismic evidence of nonlinear crustal deformation during a large slow slip event in Mexico, *Geophys. Res. Lett.* **38,** no. 8, doi: 10.1029/2011GL047151.

Rivière, J., Z. Lv, P. A. Johnson, and C. Marone (2018). Evolution of b-value during the seismic cycle: Insights from laboratory experiments on simulated faults, *Earth Planet. Sci. Lett.* **482,** 407–413.

Rouet-Leduc, B., C. Hulbert, D. C. Bolton, C. X. Ren, J. Riviere, C. Marone, R. A. Guyer, and P. A. Johnson (2018). Estimating fault friction from seismic signals in the laboratory, *Geophys. Res. Lett.* **45,** no. 3, 1321–1329.

Rouet-Leduc, B., C. Hulbert, N. Lubbers, K. Barros, C. J. Humphreys, and P. A. Johnson (2017). Machine learning predicts laboratory earthquakes, *Geophys. Res. Lett.* **44,** no. 18, 9276–9282.

Rousseeuw, P. J. (1987). Silhouettes: A graphical aid to the interpretation and validation of cluster analysis, *J. Comput. Appl. Math.* **20,** 53–65.

Scholz, C. H. (1968). The frequency–magnitude relation of microfracturing in rock and its relation to earthquakes, *Bull. Seismol. Soc. Am.* **58,** no. 1, 399–415.

Scuderi, M. M., C. Marone, E. Tinti, G. Di Stefano, and C. Collettini (2016). Precursory changes in seismic velocity for the spectrum of earthquake failure modes, *Nature Geosci.* **9,** no. 9, 695–700, doi: 10.1038/NGEO2775.

Tan, P. N., M. Steinbach, and V. Kumar (2006). Cluster analysis: basic concepts and algorithms, in *Introduction to Data Mining*, Vol. 8, Addision-Wesley, Boston, Massachusetts, 487–568.

Tinti, E., M. M. Scuderi, L. Scognamiglio, G. Di Stefano, C. Marone, and C. Collettini (2016). On the evolution of elastic properties during laboratory stick-slip experiments spanning the transition from slow slip to dynamic rupture, *J. Geophys. Res.* **121,** no. 12, 8569–8594.

Weeks, J., D. Lockner, and J. Byerlee (1978). Change in b-values during movement on cut surfaces in Granite, *Bull. Seismol. Soc. Am.* **68,** no. 2, 333–341.

Wu, Y., Y. Lin, Z. Zhou, D. C. Bolton, J. Liu, and P. Johnson (2018). DeepDetect: A cascaded region-based densely connected network for seismic event detection, *IEEE Trans. Geosci. Remote Sens.* **99,** 1–14.

Xie, S., T. H. Dixon, D. Voytenko, D. M. Holland, D. Holland, and T. Zheng (2016). Precursor motion to iceberg calving at Jakobshavn Isbræ, Greenland, observed with terrestrial radar interferometry, *J. Glaciol.* **62,** no. 236, 1134–1142, doi: 10.1017/jog.2016.104.

David C. Bolton
Chris Marone
Department of Geosciences
Pennsylvania State University
201 Old Main

University Park, Pennsylvania 16802 U.S.A.
dcb31@psu.edu
chrisjmarone@gmail.com

Parisa Shokouhi
Jacques Rivière
Department of Engineering Science and Mechanics
Pennsylvania State University
201 Old Main
University Park, Pennsylvania 16802 U.S.A.
pxs990@psu.edu
jvr5626@psu.edu

Bertrand Rouet-Leduc
Claudia Hulbert
Paul A. Johnson
Geophysics Group
Los Alamos National Laboratory
30 Bikini Atoll Road
Los Alamos, New Mexico 87545 U.S.A.
bertrand.rouetleduc@gmail.com
claudia.hulbert@gmail.com
paj@lanl.gov